

Numerical attoclock on atomic and molecular hydrogen

Vladislav V. Serov,¹ Alexander W. Bray,² and Anatoli S. Kheifets^{2,*}

¹ *Department of Theoretical Physics, Saratov State University, Saratov 410012, Russia*

² *Research School of Physical Sciences, The Australian National University, Canberra ACT 0200, Australia*

(Dated: March 17, 2022)

Numerical attoclock is a theoretical model of attosecond angular streaking driven by a very short, nearly a single oscillation, circularly polarized laser pulse. The reading of such an attoclock is readily obtained from a numerical solution of the time-dependent Schrödinger equation as well as a semi-classical trajectory simulation. By making comparison of the two approaches, we highlight the essential physics behind the attoclock measurements. In addition, we analyze the predictions the Keldysh-Rutherford model of the attoclock [Phys. Rev. Lett. **121**, 123201 (2018)]. In molecular hydrogen, we highlight a strong dependence of the width of the attoclock angular peak on the molecular orientation and attribute it to the two-center electron interference. This effect is further exemplified in the weakly bound neon dimer.

PACS numbers: 32.80.-t, 32.80.Fb

The experimental technique of attosecond angular streaking (attoclock) is based on measuring an offset angle of the peak photoelectron momentum distribution (PMD) in the polarization plane of a close-to-circularly polarized laser pulse. The attoclock attempts to relate this offset angle with the time the tunneling electron spends under the barrier (tunneling time) [1–4]. As the tunneling is an exponentially suppressed process, it occurs predominantly at the peak of the driving laser pulse. At this instant, the electric field is aligned with the major axis of the polarization ellipse. The photoelectron emerges from the tunnel with the zero velocity and its canonical momentum captures the vector potential of the laser field at the time of exit. This momentum is carried to the detector and its angular displacement relative to the minor polarization axis is converted to the tunneling time $\tau = \theta_A/\omega$, where ω is the angular frequency of the driving field. A similar attoclock reading θ_A can be obtained from numerical simulations with very short, nearly single oscillation, circularly polarized pulses. The utility of such a “numerical attoclock” is that it allows for treatment by various simplified, but more physically transparent, techniques such as an analytic R -matrix theory [5], a classical back-propagation analysis [6], classical-trajectory Monte Carlo simulations [7] and a classical Rutherford scattering model [8]. By making comparison with these models, numerical attoclock experiments firmly point to a vanishing tunneling time [5, 6, 8]. Similar conclusion was also reached in recent theoretical [9, 10] and experimental [11] works. The debate of the finite tunneling time is still open. Some authors continue to advocate a finite tunneling time [12–14] while others suggest that the whole concept is ill defined and no meaningful definition of the tunneling time can be given [15].

Irrespective of the answer to the tunneling time conundrum, the principle of attoclock remains appealing and finds its application to more complex targets. In particular, there have been preliminary reports of attosecond angular streaking measurements on molecular hydrogen [16, 17]. Coincident detection of photoelectrons and molecular fragments in dissociative ioniza-

tion of H_2 allows to conduct attoclock measurements on aligned molecules and to explore the effect of molecular orientation.

To highlight the essential physics behind the attoclock measurements on H_2 and to contrast them with analogous measurements on the hydrogen atom, we employ the same principle of the numerical attoclock. We solve the time-dependent Schrödinger equation (TDSE) driven by a short, nearly single-cycle, circularly polarized laser pulse. In parallel, we simulate the numerical attoclock within the strong field approximation (SFA) by performing the steepest descent integration using the saddle point method (SPM) [18, 19]. With such a short driving pulse, this analysis is streamlined and the whole PMD can be obtained from the contribution of just a single strongly dominant saddle point.

We find the attoclock offset angles of the H atom and the H_2 molecule to be rather similar, the latter only weakly dependent on the molecular axis orientation relative to the polarization plane. We interpret these results within the so-called Keldysh-Rutherford (KR) model [8] in which the photoelectron undergoes elastic scattering on the Coulomb potential of the residual ion. The point of the closest approach in this model is equated with the Keldysh tunnel width $b = I_p/E_0$ expressed via the ionization potential I_p and the peak electric field E_0 . At the laser pulse intensities under consideration $E_0 \ll 1$ a.u. Thus the tunnel width is significantly larger than the inter-atomic distance $b \gg R$. Hence, the molecular orientation is of little effect. In contrast, the angular width of the photoelectron peak, both in and out of the polarization plane, is markedly different for H and H_2 . More importantly, this width depends strongly on the molecular axis orientation and bears a clear signature of the two-center electron interference. Such an interference has been predicted theoretically for single-photon molecular ionization [20, 21]. It had been observed in various molecular ionization processes and, more recently, in strong field phenomena including high order harmonic generation and above threshold ionization [22–27]. This effect is further exemplified in weakly bound noble gas clusters where it depends sensitively on the symmetry of the dissociative ionic state [28]. We confirm it here by conducting the SPM calculations on the Ne_2 dimer.

The rest of the paper is organized as follows. In Sec. I we describe our quantum-mechanical (IA) and

*Electronic address: A.Kheifets@anu.edu.au

semi-classical (IB) techniques. In Sec. II we present the results of our simulations on atomic (II A) and molecular (II B) hydrogen. In Sec. II A we also compare the results of numerical [8] and real [11] attoclock experiments and highlight the range of validity of the KR model. We also make a comparison of the TDSE and SFA-SPM predictions for numerical attoclock. This comparison exemplifies the role of the Coulomb field of the residual ion. In Sec. II B we compare the readings of the atomic and molecular attoclocks and attribute their difference to the two-center Young-type interference. This interference is manifested much stronger in a weakly bound and very extended neon dimer Ne_2 which we consider in Sec. II C.

I. METHODS AND TECHNIQUES

A. Quantum mechanical simulations

We solve numerically the TDSE

$$i\partial\Psi(\mathbf{r})/\partial t = [\hat{H}_{\text{target}} + \hat{H}_{\text{int}}(t)]\Psi(\mathbf{r}), \quad (1)$$

where \hat{H}_{target} describes a one-electron target in the absence of the applied field and the interaction Hamiltonian is written in the velocity gauge

$$\hat{H}_{\text{int}}(t) = \mathbf{A}(t) \cdot \hat{\mathbf{p}}, \quad \mathbf{E}(t) = -\partial\mathbf{A}/\partial t. \quad (2)$$

Here the vector potential of the driving pulse is

$$\mathbf{A}(t) = \frac{A_0}{\sqrt{\epsilon^2 + 1}} \cos^4(\omega t/2N + \phi) \begin{bmatrix} \cos(\omega t) \\ \epsilon \sin(\omega t) \end{bmatrix} \quad (3)$$

with the ellipticity parameter ϵ , the angular frequency ω and the carrier envelope phase (CEP) ϕ . The pulse length is parametrized with the number of optical cycles N and \mathbf{A} vanishes for $|t| \geq N\pi/\omega$. Note that for $\phi = 0$, the center of the pulse corresponds to $t = 0$. The (peak) field intensity is given by $I = 2(\omega A_0)^2$ and the frequency ω is taken to correspond to 800 nm radiation. The single-oscillation pulse employed in the present work corresponds to $\epsilon = 1$, $N = 2$ and $\phi = 0$. In contrast, multi-cycle pulses with $\epsilon = 0.88$, $N = 5$ and various ϕ were employed in numerical simulations of the real experiment [11]. It appears that the effect of the driving pulse shape on the attoclock reading θ_A is very significant as will be highlighted in Sec. II A.

In the case of atomic hydrogen, TDSE (1) was solved by two different numerical techniques: the iSURF method [29] and the split-operator method [30]. The iSURF method was used previously both for numerical attoclock [8] and real experiment [11] simulations. A similar set of numerical parameters was employed as in the previous works. The two TDSE codes [29, 30] were benchmarked against each other and the numerical attoclock results were found to be identical. The split-operator method [30] was also adapted for molecular hydrogen. The H_2 molecule at the equilibrium internuclear distance $R = 1.4$ a.u. was treated within the single active electron approximation on the frozen-core Hartree-Fock (HF) basis [30]. The radial integration was conducted by the finite-element method on the Gauss-Lobatto quadratures. The radial grid parameters were chosen as follows:

the finite element order $N_{\text{ORD}} = 4$, the number of finite elements $N_{\text{FE}} = 91$, the radial step $\Delta r = 1$ a.u. to the radial boundary $r_{\text{max}} = 91$ a.u. The total number of the radial basis functions was $N_r = 364$. An unphysical reflection from the upper radial boundary was suppressed by the exterior complex scaling (ECS). The ECS parameters were as follows: $r_{\text{ECS}} = 51$ a.u. and $\theta_{\text{ECS}} = 30^\circ$. The angular variables were treated separately with the number of azimuthal and polar points $N_\theta = 64$ and $N_\phi = 128$, respectively. Unlike in the previous work [30], we employ here the spherical rather than spheroidal coordinates as a sufficiently large angular basis was used to approximate the photoelectron wave packet far away from the origin. The ionization amplitude was extracted from the time-dependent wave function using the time-corrected flux (t-SURFFc) method) through a surface of a sufficiently large radius $r_S = 50$ a.u.

A typical 2D momentum distribution in the polarization plane $P(k_x, k_y, k_z = 0)$ is shown for atomic hydrogen on the top panel of Fig. 1. This distribution is integrated radially to obtain the angular distribution $P(\theta) = \int k dk P(k_x, k_y, k_z = 0)$. It is then fitted with a Gaussian $P(\theta) \propto \exp[(\theta - \theta_A)^2/\mathcal{W}^2]$ to determine the peak position and this value is assigned to the attoclock offset angle θ_A . The symmetry of $P(\theta)$ relative to θ_A is carefully monitored and serves as a test of the quality of the TDSE calculation. We also analyze the Gaussian width \mathcal{W} of this distribution.

B. Semi-classical approach

We follow [18, 19] and write the ionization amplitude as

$$D(\mathbf{k}) = -i \sum_{s=1}^{N_{\text{SP}}} \left\{ \frac{2\pi i}{\mathbf{E}(t_s) \cdot [\mathbf{k} + \mathbf{A}(t_s)]} \right\}^{1/2} \times \langle \mathbf{k} + \mathbf{A}(t_s) | \mathbf{r} \cdot \mathbf{E}(t_s) | \psi_0 \rangle \exp[iS_{\mathbf{k}}(t_s)], \quad (4)$$

where $S_{\mathbf{k}}(t) = \int^t dt' \{ [\mathbf{k} + \mathbf{A}(t')]^2/2 + I_p \}$ is the semiclassical action and, for hydrogenic targets,

$$\langle \mathbf{k} | \mathbf{r} \cdot \mathbf{E}(t) | \psi_0 \rangle = -i2^{7/2}(2I_p)^{5/4} \frac{\mathbf{k} \cdot \mathbf{E}(t)}{\pi(\mathbf{k}^2 + 2I_p)^3}. \quad (5)$$

The summation in Eq. (4) is carried over the saddle points t_s that are solutions of the saddle point equation

$$\partial S_{\mathbf{k}}(t_s)/\partial t = [\mathbf{k} + \mathbf{A}(t_s)]^2/2 + I_p = 0. \quad (6)$$

Combining Eqs. (4)-(5) under condition (6) leads to

$$D(\mathbf{k}) = -2^{-1/2}(2I_p)^{5/4} \sum_{s=1}^{N_{\text{SP}}} \left[S''_{\mathbf{k}}(t_s) \right]^{-1} \exp[iS_{\mathbf{k}}(t_s)]. \quad (7)$$

The real part of the saddle points $\text{Re } t_s$ specify those times when the electron exits the tunnel to reach the detector with the drift momentum \mathbf{k} . For circular polarization, the number of the saddle points $N_{\text{SP}} = N + 1$, where N is the number of the pulse oscillations [19]. With the presently chosen envelope, $N_{\text{SP}} = 3$ of which only one dominant SP makes the overwhelming contribution to the PMD shown on the bottom panel of Fig. 1.

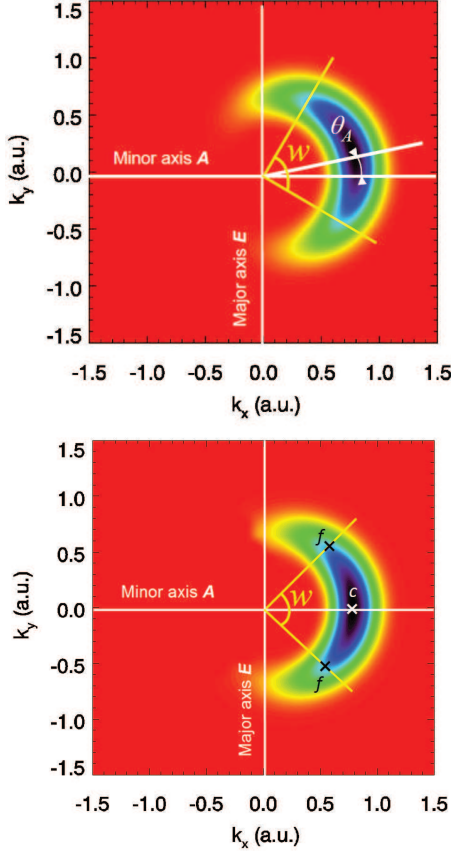


FIG. 1: Photoelectron momentum distribution $P(k_x, k_y, k_z = 0)$ of the atomic hydrogen in the polarization plane at the driving field intensity $I = 8 \times 10^{13} \text{ W/cm}^2$. The attoclock offset angle θ_A and the angular width \mathcal{W} are marked. The coloration ranges from zero (red) to the maximum (black) linearly. Results of the TDSE (top) and SPM (bottom) calculations are displayed. The c and f labels on the bottom panel are used to mark the center and fringes of the PMD.

These saddle points are mapped on the parametric plot of the vector potential $\mathbf{A}(t)$ in the polarization plane shown on the top panel of Fig. 2. Here the momenta $\hat{\mathbf{k}}$ corresponding to the center c and fringes f of the PMD displayed on the bottom panel of Fig. 1 are drawn with straight lines. In the absence of the ionization potential, $\mathbf{k} = -\mathbf{A}(t_s)$, the saddle points are entirely real and can be mapped on the intersection of the momentum and the vector potential lines. With a finite ionization potential, the saddle points acquire an imaginary part and deviate from the $\hat{\mathbf{k}}$ vector direction. This imaginary part $\text{Im } t_s$ dampens the contribution of a given saddle point exponentially. In Fig. 2 we depict this relation via the point size which is proportional to $\exp(-\text{Im } t_s)$ normalised to that of the dominant, center saddle point. The minor saddle points near the origin have large $\text{Im } t_s$ and hence their marks are not visible in the scale of the figure. The relative size of the fringe saddle points affects the angular width of the PMD. The larger is $\text{Im } t_s$ and the smaller the dots at the fringes relative to that at the center, the smaller is the width.

In the case of the H_2 molecule, the SP equations (6) and (7) require modification [31]. The ground state wave function is expressed as a linear combination of the hydrogenic orbitals $\psi_0 = C_\psi \sum_{j=1,2} \phi[\mathbf{r} + (-1)^j \mathbf{R}/2]$, where j is the atomic site index, \mathbf{R} is the internuclear

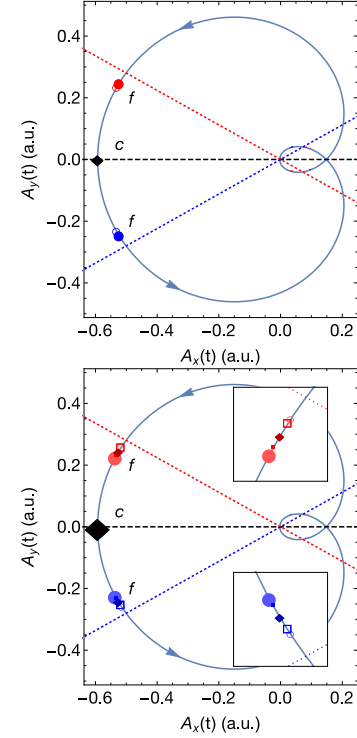


FIG. 2: Saddle point solutions corresponding to the fringes f (blue/red) and center c (black) of the PMD as marked on the bottom panel of Fig. 1. The direction of each of the chosen momenta $\hat{\mathbf{k}}$ are given by dashed lines of the matching color. Top: atomic hydrogen (6) with $k_z = 0.0 \text{ a.u.}$ (filled circles) and $k_z = 1.0 \text{ a.u.}$ (open circles). Bottom: molecular hydrogen with $j = 1, 2$ (9) given by filled and open symbols, respectively. The perpendicular orientation is given with diamonds of dark hue, the major axis orientation with circles of light hue, and the minor axis orientation with squares of standard hue. The insets highlight the solutions about each fringe.

separation vector, and C_ψ is the overlap of the orbitals centered on the two atomic sites. Accordingly, the ionization amplitude is written as a coherent sum

$$D(\mathbf{k}) = \sum_{j=1,2} D_j(\mathbf{k}, t_s) \exp[(-1)^j i \mathbf{k} \cdot \mathbf{R}/2] . \quad (8)$$

Here $D_j(\mathbf{k}, t_s)$ denotes the ionization amplitude (7) evaluated at the saddle point t_s found as a solution of the modified SP equation

$$[\mathbf{k} + \mathbf{A}(t_s)]^2/2 + I_p - (-1)^j \mathbf{E}(t_s) \cdot \mathbf{R}/2 = 0 . \quad (9)$$

The difference between the atomic SP equation (6) and its molecular counterpart (9) is in the potential energy term $\pm \mathbf{E}(t_s) \cdot \mathbf{R}/2$. This term defines the energy gain or loss for the electron to travel to the molecule mid point and has the opposite signs for different atomic sites. Accordingly, the single dominant SP in the atomic case is split into two points as illustrated graphically on the right panel of Fig. 2. The corresponding factor $\exp[\pm i \mathbf{k} \cdot \mathbf{R}/2]$ in the ionization amplitude (8) defines the phase difference between the two wave packets emitted from different atomic sites. We note that the molecular terms in both Eqs. (8) and (9) vanish when the molecule is aligned perpendicular to the polarization plane.

II. RESULTS

A. Atomic hydrogen

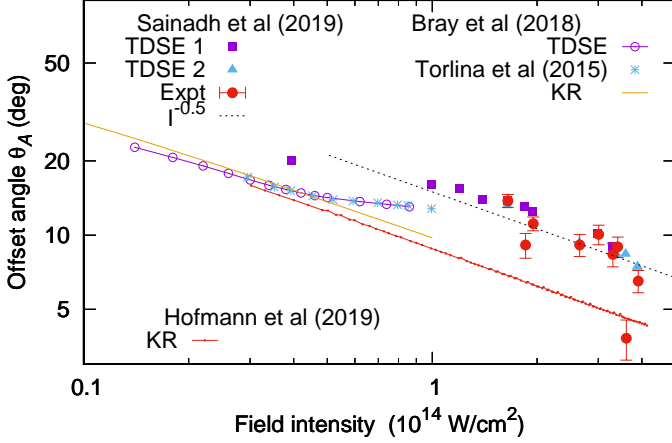


FIG. 3: The attoclock offset angle θ_A plotted as a function of the laser field intensity. The TDSE1 (red squares) and TDSE2 (blue triangles) calculations and the experimental points (with error bars) visualize the data of Sainadh et al. [11] obtained with multi-cycle pulses. The TDSE calculation (red open circles) and the KR model prediction (red solid line) from Bray et al. [8] refer to the single-oscillation pulses. Similar calculation of Torlina et al. [5] (blue asterisks) is also shown. The KR model is extended beyond the range of its validity by Hofmann et al. [32] and displayed with the thick dotted line. The thin dotted line fits the data of Sainadh et al. [11] with the characteristic field intensity dependence $I^{-0.5}$ predicted by the KR model.

The attoclock offset angles θ_A as functions of the field intensity under different driving pulse conditions are exhibited in Fig. 3. Here we display the experimental and theoretical results of Sainadh et al. [11] obtained with multi-cycle CEP averaged pulses. The presently employed iSURF code was calibrated against the TDSE1 and TDSE2 calculations of Sainadh et al. [11] at several field intensity and CEP values. The corresponding results were found to be fully compatible. In the same figure, we present the TDSE calculations with single-oscillation pulses [5, 8] which are very similar to each other but deviate noticeably from the TDSE1 and TDSE2 results corresponding to CEP averaged multi-cycle elliptical pulses. In the low field intensity range, the TDSE results merge the predictions of the KR model [8] which was designed to explain a very steep rise of the offset angle θ_A with decreasing laser pulse intensity. It was tempting to explain this rise in terms of the increasing tunnel with and corresponding increase of the tunneling time. However, in reality, this is an effect of the stronger elastic scattering of a slower photoelectron in the Coulomb field of the residual ion. We note that the KR model deviates noticeably from the TDSE at an increasing laser field. It is therefore meaningless to extend it to very large intensities as was done in [32]. Moreover, it is even less meaningful to explain the difference between the KR predictions and the experiment by a finite tunneling time as was suggested in [32]. The offset angles became virtually zero when the long-range Coulomb field

was replaced by a short-range Yukawa potential in both TDSE1 and TDSE2 calculations [11].

The main difference between the PMD shown on the top and bottom panels of Fig. 1 is that $\theta_A = 0$ in the SFA and SPM. This is another indication that the main contribution to the attoclock offset angle comes from the Coulomb field of the residual ion which is not included in the SFA. Except for this offset angle, the overall structure of the PMD in the polarization plane is reproduced remarkably well by the SPM. We quantify this PMD by its angular width \mathcal{W} which we extract from the Gaussian fitting to the radially integrated momentum density. The width parameter extracted from the TDSE and SPM calculations are shown in Fig. 4. On the top panel, we show the width $\mathcal{W}(I)$ in the polarization plane as a function of the field intensity I . We observe that this dependence is not monotonous. This feature can be qualitatively understood from the SFA formulas given in [33] for a continuous elliptical field. In this case, the SP equation (6) can be solved analytically. For strong fields, when the Keldysh adiabaticity parameter $\gamma \ll 1$, the angular width grows with intensity as $\mathcal{W} \propto 1/\sqrt{\gamma} \propto I^{1/4}$. In the opposite limit $\gamma \gg 1$ the width is falling with intensity as $\mathcal{W} \propto \sqrt{\ln(c\gamma)}$ with $c = 2/(1 - \xi^2)^{1/2}$ expressed via the ellipticity parameter ξ . The cross-over between these falling and rising intensity dependence of the width occurs around $\gamma \simeq 1$.

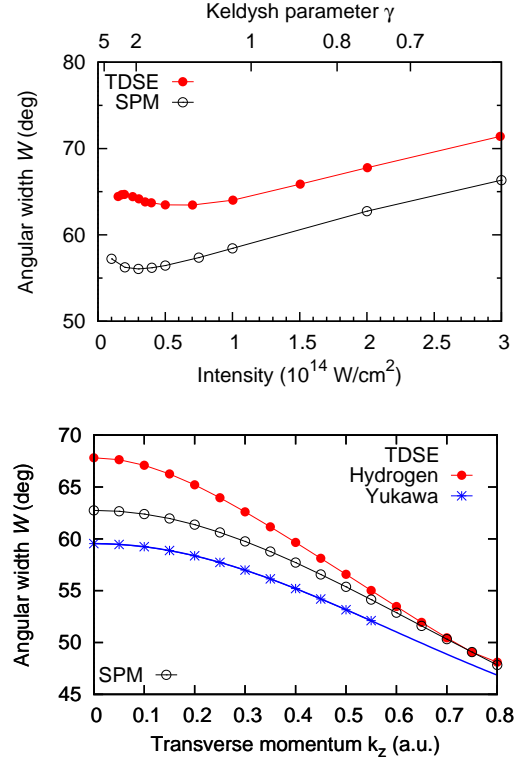


FIG. 4: Top: Angular width $\mathcal{W}(I)$ of the PMD of atomic hydrogen in the polarization plane as a function of the field intensity I . Bottom: The width parameter $\mathcal{W}(k_z)$ as a function of the transverse photoelectron momentum outside the polarization plane at the field intensity of 2×10^{14} W/cm².

On the bottom panel of Fig. 4 we display the width dependence on the transverse momentum outside the polarization plane $\mathcal{W}(k_z)$ at a fixed field intensity. We see that the width is rapidly falling with increasing k_z . A significant part of this fall is reproduced by the SPM cal-

culation simply because the SP equation (6), which can be understood as the energy conservation at the exit from the tunnel, contains an additional kinetic energy term $k_z^2/2$. This increases an effective ionization potential [34] and thus reduces $\text{Im } t_s$ as illustrated on the top diagram of Fig. 2 (filled symbols at $k_z = 0$ versus open symbols at $k_z = 1$ au). Hence the angular width decreases. The effect of the Coulomb field of the proton is seen clearly from comparison of the two TDSE calculations on the hydrogen and Yukawa atoms. In the latter case, the Coulomb field is screened $V(r) = -(Z^*/r) \exp(-r/2)$ with $Z^* = 1.47$ to maintain identical ionization potentials. The TDSE calculation on the Yukawa atom is particularly close to the SPM result. Such a calculation also exhibits a zero angular offset $\theta_A = 0$ [5, 8, 11].

B. Molecular hydrogen

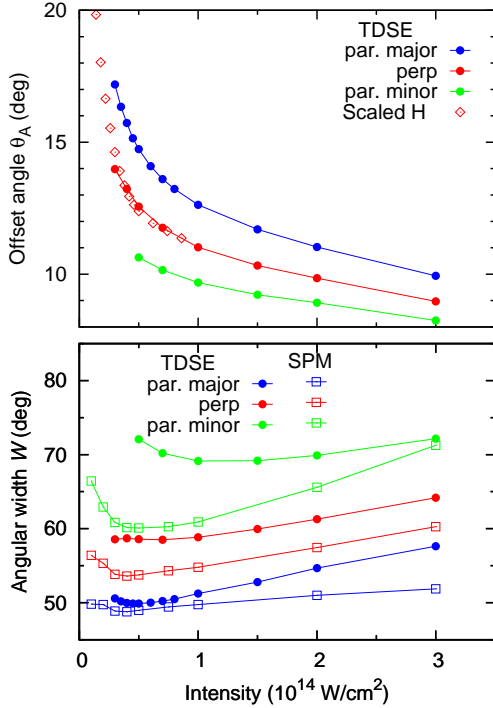


FIG. 5: The attoclock offset angle θ_A (top) and the angular width W (bottom) of the H_2 molecule as functions of the field intensity. The molecule is aligned perpendicular to the polarization plane (shown with red symbols), aligned with the peak E field (“major” \hat{e}_y axis, blue symbols) and with the peak A potential (“minor” \hat{e}_x axis, green symbols). The top panel shows the offset angle θ_A of the H atom scaled to the ionization potential of H_2 .

We illustrate the effect of the molecular orientation in Fig. 5 where we show the attoclock offset angle θ_A (top) and the angular width parameter W (bottom) for the H_2 molecule in three orientations: perpendicular to the polarization plane (shown with red symbols), aligned with the peak E field (“major” \hat{e}_y axis, blue symbols) and with the peak A potential (“minor” \hat{e}_x axis, green symbols). Both the TDSE and SPM results are shown for the width parameter (filled circles and open squares, respectively). We observe on the top panel that the attoclock offset angles θ_A vary minorly with the molecular orientation. On the same panel we plot the corresponding offset angles of the atomic hydro-

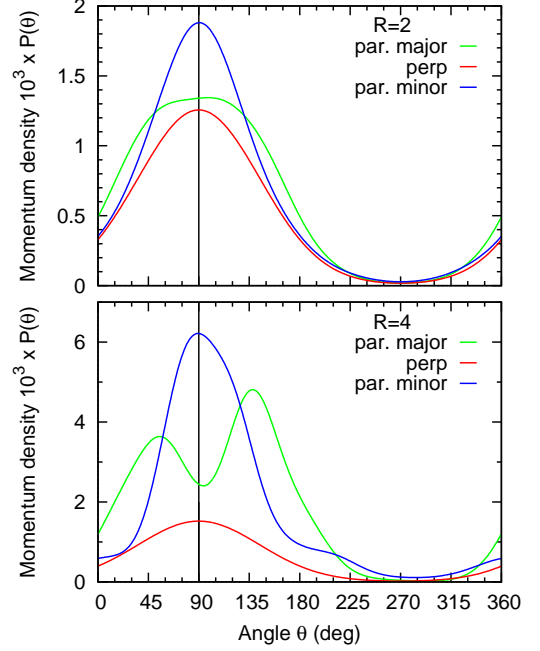


FIG. 6: Radially integrated PMD $P(\theta)$ in the polarization plane for the three orientations of the Yukawa molecule with $R = 2$ a.u. (top) and 4 a.u. (bottom).

gen. According to the KR model, the offset angle due to the scattering in the Coulomb potential is estimated as $\theta_A = (\omega^2/E_0)(Z/I_p)$, where Z is an effective charge of the residual ion. To bring the offset angle of the hydrogen atom to the H_2 scale, we need to multiply it by the corresponding ionization potentials ratio $\theta_A^H \times I_p^H/I_p^{H_2}$, where for the H_2 molecule we take the HF ionization potential $I_p^{H_2} = 15.6$ eV. We see that such a scaled atomic hydrogen calculation is almost indistinguishable from the H_2 results in the perpendicular orientation for which the interference terms vanish.

The angular width W varies very significantly depending on the molecular orientation. This behaviour is similar in the TDSE and SPM calculations. The latter model allows for the understanding of this behavior qualitatively in terms of the two-center interference through analysis of the underlying saddle points, illustrated in the right panel of Fig. 5. For a given in-plane orientation the interference term in Eq. (9) effectively increases (decreases) the ionization potential thus increasing (or decreasing) the $\text{Im } t_s$ and relative contribution of the corresponding saddle points.

More insight into the orientation dependence of the attoclock width W can be gained from a model Yukawa molecule in which the two Yukawa atoms are placed at a varying distance. Results of the TDSE calculation for such a target are exhibited in Fig. 6. Here we display the angular distribution $P(\theta)$ of the radially integrated PMD in the polarization plane for alternate molecular orientations and the two inter-atomic distances of $R = 2$ and 4 a.u. For the “major” axis molecular alignment, the potential energy term in the SP equation (9) is large. It suppresses photoemission from one atomic site and enhances it from another. The enhanced photoelectron wave packet has a smaller angular width which is carried through to the detector. For the “minor” axis alignment, the two photoelectron wave packets have the same width but are displaced relative to the detection direction of

90° to the opposite sides. This results in a visibly non-Gaussian shape and a considerable increase of the width of the PMD at a small separation $R = 2$ a.u. evolving into two split peaks at a larger separation $R = 4$ a.u. A non-gaussian shape of the PMD may explain why the agreement of the TDCS and SPM calculations for the “major” and “minor” axis alignment on the bottom panel of Fig. 5 is poorer than for perpendicular molecular orientation. Lack of symmetry of the PMD peak relative to the 90° direction may also explain a small deviation of the attoclock offset angles at different molecular orientations visible on the top panel of Fig. 5.

C. Neon dimer

The hint of the two-center Young-type interference in H_2 , which manifests itself as the orientation dependent angular width \mathcal{W} , is greatly exemplified in a model Yukawa molecule with an enlarged inter-atomic distance. This enlargement happens naturally in weakly bound noble gas dimers held by weak van der Waals forces. Consequently, the photoelectron momentum distribution shows a very distinct interference pattern. This pattern depends strongly on the symmetry of the molecular orbital being ionized which is captured by the kinetic energy release (KER) from the corresponding ionic dissociative state [28].

In these measurements, performed on the Ne_2 dimer with a long, 40 fs circularly polarized laser pulse, the KER of the dissociating atomic fragments were analyzed. Thus, the gerade $2p\sigma_g$ and ungerade $2p\sigma_u$ orbitals of the molecular ground state could be readily resolved by their distinctively different KER. It was argued that the corresponding two-center interference factor

$$P \propto \cos^2 \left(\mathbf{k} \cdot \frac{\mathbf{R}}{2} + \frac{\Delta\phi}{2} \right) \quad (10)$$

should contain the phase difference $\Delta\phi = \pi$ (gerade) and 0 (ungerade), accordingly. When the two symmetries are mixed, the fringes and anti-fringes overlap and the interference pattern is washed away.

This behavior is seen on the top panel of Fig. 7 where we generate an atomic-like momentum distribution in the polarization plane of a continuous circularly polarized field. Here we take the ionization potential of the Ne atom $I_p = 21.6$ eV, $\omega = 0.0584$ a.u. ($\lambda = 780$ nm), peak intensity 7.3×10^{14} W/cm², and employ the analytical SPM formula given by Eq. (27) of [33] multiplied by a spherical harmonic.

We then take the atomic ionization amplitude and insert it into the molecular expression (8) with $\mathbf{R} = 5.85\hat{e}_x$ a.u. and get the momentum distribution shown in the middle panel of Fig. 7. If we drop the $(-1)^j$ factor in Eq. (8), we generate the momentum distribution shown on the bottom pane. The keeping and dropping of the phase factor $(-1)^j$ in Eq. (8) is equivalent to selecting the phase difference $\Delta\phi = \pi$ and 0, accordingly. We find these three distinctively different distributions to correspond very closely with the experimental plots shown in the inset of Fig. 1, and Figs. 2(b) and 2(e) of [28], respectively.

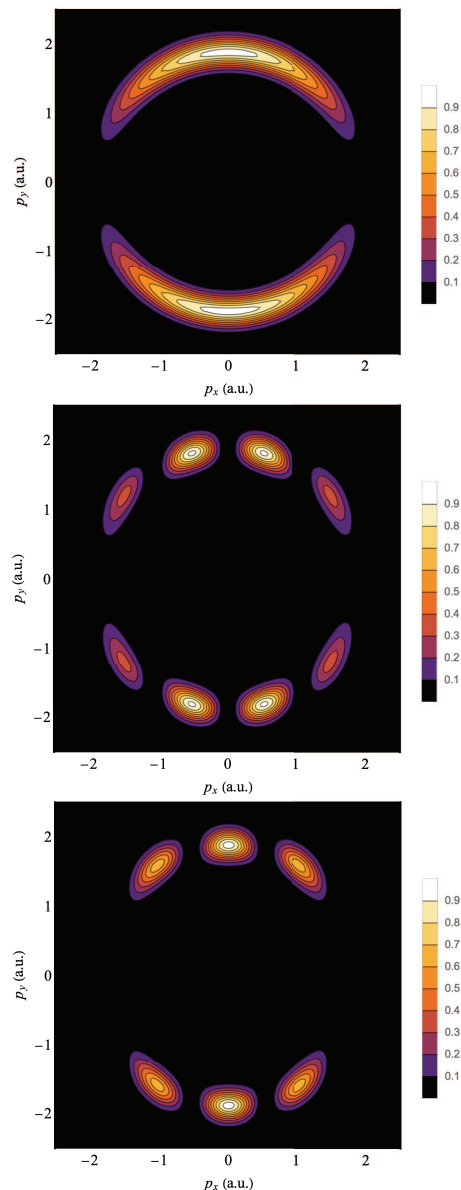


FIG. 7: Photoelectron momentum distribution in Ne_2 in the polarization plane of the circularly polarized continuous laser field. Top: atomic-like SPM calculation using analytic expressions of [33]. Middle and bottom: the same calculation modulated by the interference factor (10) with the phase difference $\Delta\phi = \pi$ (gerade) and 0 (ungerade), respectively.

III. CONCLUSION

In conclusion, we conducted a numerical study of attoclock on atomic and molecular hydrogen driven by a single-cycle circularly polarized laser pulse. We interpreted our numerical results using the simplified semi-classical SPM and the classical KR models. The latter model treats the attoclock as a “nano-ruler” and relates the offset angle of the peak photoelectron momentum distribution with the tunnel width rather than the tunneling time. We explore the range of validity of the KR model and compared theoretical and experimental results obtained with short, nearly single-oscillation, and longer multi-oscillation pulses. By analyzing the width of the photoelectron momentum distribution in the H_2 attoclock, we found a clear signature of the two-center electron interference. This celebrated effect has many

decades of history but it is the present work that revealed it for the molecular attoclock. The interference effect is encoded in the molecular saddle point equation (9) and reflects the bonding or anti-bonding nature of the molecular ground state. We demonstrated this effect in the H_2 molecule, an artificially enlarged Yukawa molecule and the naturally extended N_2 dimer which has a very large inter-atomic separation.

The authors are greatly indebted to Serguei Patchkovskii who placed his iSURF TDSE code at their disposal.

The authors wish to thank Satya Sainadh, Igor Litvinyuk, Robert Sang and Sebastian Eckart for many stimulating discussions. Resources of the National Computational Infrastructure were employed.

-
- [1] P. Eckle *et al*, *Attosecond angular streaking*, Nat. Phys. **4**, 565 (2008).
 - [2] P. Eckle *et al*, *Attosecond ionization and tunneling delay time measurements in helium*, Science **322**(5907), 1525 (2008).
 - [3] A. N. Pfeiffer, C. Cirelli, M. Smolarski, D. Dimitrovski, M. Abu-samha, L. B. Madsen, and U. Keller, *Attoclock reveals natural coordinates of the laser-induced tunnelling current flow in atoms*, Nat Phys **8**, 76 (2012).
 - [4] A. S. Landsman, M. Weger, J. Maurer, R. Boge, A. Ludwig, S. Heuser, C. Cirelli, L. Gallmann, and U. Keller, *Ultrafast resolution of tunneling delay time*, Optica **1**(5), 343 (2014).
 - [5] L. Torlina, F. Morales, J. Kaushal, I. Ivanov, A. Kheifets, A. Zielinski, A. Scrinzi, H. G. Muller, S. Sukiasyan, M. Ivanov, et al., *Interpreting attoclock measurements of tunnelling times*, Nat. Phys. **11**, 503 (2015).
 - [6] H. Ni, U. Saalmann, and J.-M. Rost, *Tunneling ionization time resolved by backpropagation*, Phys. Rev. Lett. **117**, 023002 (2016).
 - [7] J. Liu, Y. Fu, W. Chen, Z. L. J. Zhao, J. Yuan, and Z. Zhao, *Offset angles of photocurrents generated in few-cycle circularly polarized laser fields*, J. Phys. B **50**(5), 055602 (2017).
 - [8] A. W. Bray, S. Eckart, and A. S. Kheifets, *Keldysh-Rutherford model for the attoclock*, Phys. Rev. Lett. **121**, 123201 (2018).
 - [9] N. Eicke and M. Lein, *Trajectory-free ionization times in strong-field ionization*, Phys. Rev. A **97**, 031402 (2018).
 - [10] I. A. Ivanov, C. Hofmann, L. Ortmann, A. S. Landsman, C. H. Nam, and K. T. Kim, *Instantaneous ionization rate as a functional derivative*, Communications Physics **1**, 81 (2018).
 - [11] U. S. Sainadh, H. Xu, X. Wang, A. Atia-Tul-Noor, W. C. Wallace, N. Douguet, A. Bray, I. Ivanov, K. Bartschat, A. Kheifets, et al., *Attosecond angular streaking and tunnelling time in atomic hydrogen*, Nature **568**, 75 (2019).
 - [12] A. S. Landsman and U. Keller, *Attosecond science and the tunnelling time problem*, Physics Reports **547**, 1 (2015).
 - [13] T. Zimmermann, S. Mishra, B. R. Doran, D. F. Gordon, and A. S. Landsman, *Tunneling time and weak measurement in strong field ionization*, Phys. Rev. Lett. **116**, 233603 (2016).
 - [14] N. Camus, E. Yakaboylu, L. Fechner, M. Klaiber, M. Laux, Y. Mi, K. Z. Hatsagortsyan, T. Pfeifer, C. H. Keitel, and R. Moshhammer, *Experimental evidence for quantum tunneling time*, Phys. Rev. Lett. **119**, 023201 (2017).
 - [15] D. Sokolovski and E. Akhmatkaya, *No time at the end of the tunnel*, Communications Physics **1**, 47 (2018).
 - [16] S. S. Undurti, *Attoclock experiments on atomic and molecular hydrogen*, Ph.D. thesis, Griffith University, Brisbane, Australia (2018), URL <http://hdl.handle.net/10072/381373>.
 - [17] W. Quan, M. Zhao, V. V. Serov, M. Z. Wei, Y. Zhou, X. Y. Lai, A. S. Kheifets, and X. J. Liu, *Attosecond angular streaking on H_2 with all-ionic fragments detection, in Photonic, Electronic, and Atomic Collisions (XXXI ICPEAC)* (Deauville, France, 2019).
 - [18] D. B. Milošević, G. G. Paulus, and W. Becker, *Phase-dependent effects of a few-cycle laser pulse*, Phys. Rev. Lett. **89**, 153001 (2002).
 - [19] D. B. Milošević, G. G. Paulus, D. Bauer, and W. Becker, *Above-threshold ionization by few-cycle pulses*, J. Phys. B **39**(14), R203 (2006).
 - [20] H. D. Cohen and U. Fano, *Interference in the photoionization of molecules*, Phys. Rev. **150**, 30 (1966).
 - [21] I. G. Kaplan and A. P. Markin, *Interference phenomena in the photoionization of molecules*, Sov. Phys. Dokl. **14**, 36 (1969).
 - [22] J. Muth-Böhm, A. Becker, and F. H. M. Faisal, *Suppressed molecular ionization for a class of diatomics in intense femtosecond laser fields*, Phys. Rev. Lett. **85**, 2280 (2000).
 - [23] C. Vozzi, F. Calegari, E. Benedetti, J.-P. Caumes, G. Sansone, S. Stagira, M. Nisoli, R. Torres, E. Heesel, N. Kajumba, et al., *Controlling two-center interference in molecular high harmonic generation*, Phys. Rev. Lett. **95**, 153902 (2005).
 - [24] S. Selstø, M. Førre, J. P. Hansen, and L. B. Madsen, *Strong orientation effects in ionization of H_2^+ by short, intense, high-frequency light pulses*, Phys. Rev. Lett. **95**, 093002 (2005).
 - [25] X. Zhou, R. Lock, W. Li, N. Wagner, M. M. Murnane, and H. C. Kapteyn, *Molecular recollision interferometry in high harmonic generation*, Phys. Rev. Lett. **100**, 073902 (2008).
 - [26] S. Baker, J. S. Robinson, M. Lein, C. C., R. Torres, H. C. Bandulet, D. Comtois, J. C. Kieffer, D. M. Villeneuve, J. W. G. Tisch, et al., *Dynamic two-center interference in high-order harmonic generation from molecules with attosecond nuclear motion*, Phys. Rev. Lett. **101**, 053901 (2008).
 - [27] B. B. Augstein and C. F. De Morisson Faria, *High-order harmonic generation in diatomic molecules: quantum interference, nodal structures and multiple orbitals*, Mod. Phys. Lett. B **26**(02), 1130002 (2012).
 - [28] M. Kunitski, N. Eicke, P. Huber, J. Köhler, S. Zeller, J. Voigtsberger, N. Schlott, K. Henrichs, H. Sann, F. Trinter, et al., *Double-slit photoelectron interference in strong-field ionization of the neon dimer*, Nature Communications **10**, 1 (2019).
 - [29] F. Morales, T. Bredtmann, and S. Patchkovskii, *iSURF: a family of infinite-time surface flux methods*, J. Phys. B **49**(24), 245001 (2016).
 - [30] V. V. Serov, *Calculation of intermediate-energy electron-impact ionization of molecular hydrogen and nitrogen using the paraxial approximation*, Phys. Rev. A **84**, 062701 (2011).
 - [31] C. C. Chirilă and M. Lein, *Strong-field approximation for harmonic generation in diatomic molecules*, Phys. Rev. A **73**, 023410 (2006).
 - [32] C. Hofmann, A. S. Landsman, and U. Keller, *Atto-*

- clock revisited on electron tunnelling time*, arXiv e-prints arXiv:1901.07015 (2019), 1901.07015.
- [33] V. D. Mur, S. V. Popruzhenko, and V. S. Popov, *Energy and momentum spectra of photoelectrons under conditions of ionization by strong laser radiation (the case of elliptic polarization)*, Sov. Phys. JETP **92**(5), 777 (2001).
- [34] S. Eckart, K. Fehre, N. Eicke, A. Hartung, J. Rist, D. Traibert, N. Strenger, A. Pier, L. P. H. Schmidt, T. Jahnke, et al., *Direct experimental access to the nonadiabatic initial momentum offset upon tunnel ionization*, Phys. Rev. Lett. **121**, 163202 (2018).